

---

# A QUANTITATIVE DESCRIPTION OF SOIL MICROSTRUCTURE USING FRACTALS

Charles Moore

Geotechnics Inc.  
912 Bryden Rd.  
Columbus, OH 43205

July 1992

Final Report

APPROVED FOR PUBLIC RELEASE; DISTRIBUTION IS UNLIMITED

19980219 156

DTIC QUALITY INSPECTED 2



**PHILLIPS LABORATORY**  
**Advanced Weapons and Survivability Directorate**  
**AIR FORCE MATERIEL COMMAND**  
**KIRTLAND AIR FORCE BASE, NM 87117-5776**

---

PL-TR-97-1128

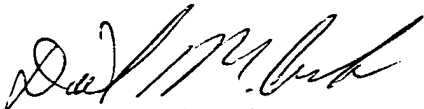
Using Government drawings, specifications, or other data included in this document for any purpose other than Government procurement does not in any way obligate the U.S. Government. The fact that the Government formulated or supplied the drawings, specifications, or other data, does not license the holder or any other person or corporation; or convey any rights or permission to manufacture, use, or sell any patented invention that may relate to them.

This report has been reviewed by the Public Affairs Office and is releasable to the National Technical Information Service (NTIS). At NTIS, it will be available to the general public, including foreign nationals.

If you change your address, wish to be removed from this mailing list, or your organization no longer employs the addressee, please notify PL/WST, 3550 Aberdeen Ave SE, Kirtland AFB, NM 87117-5776.

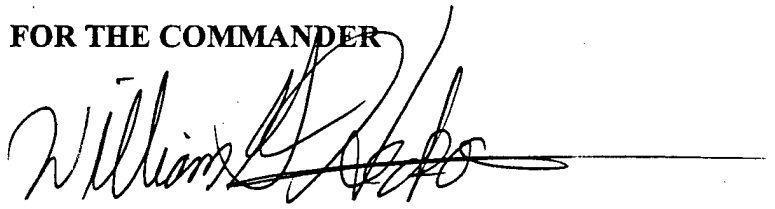
Do not return copies of this report unless contractual obligations or notice on a specific document requires its return.

This report has been approved for publication.

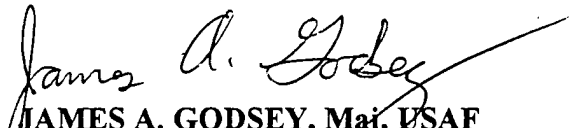


**DAVID M. CROOK**  
Project Manager

**FOR THE COMMANDER**



**WILLIAM G. HECKATHORN, Col, USAF**  
Director, Advanced Weapons and  
Survivability Directorate



**JAMES A. GODSEY, Maj, USAF**  
Chief, Tactical Warfare Applications  
Branch

# REPORT DOCUMENTATION PAGE

Form Approved  
OMB No. 0704-0188

Public reporting burden for this collection of information is estimated to average 1 hour per response, including the time for reviewing instructions, searching existing data sources, gathering and maintaining the data needed, and completing and reviewing the collection of information. Send comments regarding this burden estimate or any other aspect of this collection of information, including suggestions for reducing this burden to Washington Headquarters Services, Directorate for Information Operations and Reports, 1215 Jefferson Davis Highway, Suite 1204, Arlington, VA 22202-4302, and to the Office of Management and Budget, Paperwork Reduction Project (0704-0188), Washington, DC 20503.

|  |  |   |  |
|--|--|---|--|
| 1. AGENCY USE ONLY (Leave blank)   | 2. REPORT DATE<br>July 1992                                | 3. REPORT TYPE AND DATES COVERED<br>Final Report; 1989 - Jul 1992   |  |
| 4. TITLE AND SUBTITLE<br>A Quantitative Description of Soil Microstructure Using Fractals  |  | 5. FUNDING NUMBERS<br>C: F29601-89-C-0069<br>PE: 65502F<br>PR: 3005<br>TA: NT<br>WU: 34   |  |
| 6. AUTHOR(S)<br>Charles Moore  |  | 8. PERFORMING ORGANIZATION<br>REPORT NUMBER   |  |
| 7. PERFORMING ORGANIZATION NAME(S) AND ADDRESS(ES)<br>Geotechnics Inc.<br>912 Bryden Rd.<br>Columbus, OH 43205   |  | 10. SPONSORING/MONITORING<br>AGENCY REPORT NUMBER<br>PL-TR-97-1128  |  |
| 9. SPONSORING/MONITORING AGENCY NAME(S) AND ADDRESS(ES)<br>Phillips Laboratory<br>3550 Aberdeen Avenue, SE<br>Kirtland AFB, NM 87117-5776  |  | 11. SUPPLEMENTARY NOTES<br>This report is published in the interest of scientific and technical information exchange. The established procedures for editing reports were not followed for this technical report. |  |
| 12a. DISTRIBUTION/AVAILABILITY STATEMENT<br>Approved for public release; distribution is unlimited.  |  | 12b. DISTRIBUTION CODE  |  |
| 13. ABSTRACT (Maximum 200 Words)<br>This Phase II SBIR report presents the results of experimental studies to determine the fractal dimension associated with soil microstructure. This was accomplished by obtaining images of samples of real soils scanned directly at 3000 dpi and 256 level of grayscales. The images were then analyzed to determine individual particles and clusters of particles. The area and perimeter values of these units were then plotted on a log-log scale from which the fractal dimension of the soil microstructure could be deduced. |  |   |  |
| 14. SUBJECT TERMS<br><br>Soil Microstructure, Fractals   |  | 15. NUMBER OF PAGES<br>54   |  |
| 17. SECURITY CLASSIFICATION<br>OF REPORT<br>Unclassified   |  | 16. PRICE CODE  |  |
| 18. SECURITY CLASSIFICATION<br>OF THIS PAGE<br>Unclassified  | 19. SECURITY CLASSIFICATION<br>OF ABSTRACT<br>Unclassified | 20. LIMITATION OF ABSTRACT<br><br>Unlimited   |  |



## CONTENTS

| <u>Section</u>   | <u>Page</u> |
|--|-------------|
| BACKGROUND   | 1           |
| PRINCIPLES OF FRACTAL GEOMETRY                               | 2           |
| DATA ACQUISITION TECHNIQUES                                  | 3           |
| DATA REDUCTION   | 5           |
| VERBAL DESCRIPTION OF SAMPLES TESTED                         | 11          |
| PICTORIAL AND QUANTITATIVE DESCRIPTION OF SAMPLES TESTED     | 13          |
| THRESHOLD IMAGERY  | 13          |
| PARTICLE SIZE DISTRIBUTION                                   | 13          |
| PARTICLE ROUGHNESS   | 13          |
| PRINCIPLES OF FRACTAL DATA ANALYSIS                          | 47          |
| ANALYTICAL CONSIDERATIONS FOR TWO OVERLAPPING CIRCULAR SPOTS | 47          |
| ANALYTICAL CONSIDERATIONS FOR TWO OVERLAPPING SQUARES        | 51          |
| ANALYTICAL CONSIDERATIONS FOR TWO OVERLAPPING DIAMONDS       | 54          |
| COMPARISON OF ANALYTICAL RESULTS                             | 57          |
| RECOMMENDED ANALYSIS PROCEDURE                               | 61          |
| ANALYSIS OF THE EXPERIMENTAL DATA                            | 62          |
| RESULTS  | 71          |
| SMALL PARTICLE ROUGHNESS                                     | 72          |
| CONCLUSIONS  | 74          |
| RECOMMENDATIONS FOR PHASE III WORK                           | 75          |
| REFERENCES   | 76          |
| APPENDICES   |             |
| A. PROCEDURE FOR IMAGE ACQUISITION AND ANALYSIS              | 77          |
| B. MATHEMATICAL DERIVATIONS (PORTIONS MISSING)               | 84          |

## FIGURES

| Figure    |  | Page    |
|-----------|--|---------|
| 1         | Typical grayscale image.                           | 7       |
| 2         | Thresholded image showing editing process.         | 9       |
| 3 - 22    | Thresholded imagery for each sample tested.        | 14 - 33 |
| 23a - 35a | Particle size distribution for each sample tested. | 34 - 46 |
| 23b - 35b | Histograms of probability for particle roughness.  | 34 - 46 |
| 36        | Typical fractal plot.                              | 48      |
| 37        | Overlapping circular spots.                        | 49      |
| 38        | Overlapping squares.                               | 53      |
| 39        | Overlapping diamonds.                              | 55      |
| 40        | Comparison of results for simple geometries.       | 58      |
| 41 - 53   | Fractal plots for each sample tested.              | 64 - 70 |
| 54        | Fractal dimension versus small particle roughness. | 73      |

(Figures are missing)

TABLE

Table

Page

1

Summary of data.

71

## BACKGROUND

This report presents the results of experimental studies to determine the fractal dimension associated with soil microstructure. The work constitutes Phase II of a Small Business Innovation Research (SBIR) project directed toward using fractal principles to describe soil microstructure. The work follows up on research initiated under Phase I (Ref. 1); nevertheless, the Phase II results as described in this report stand independently of Phase I work.

The scope of work for this task of Phase II consisted of:

1. Obtaining images of samples of real soils in a format suitable for image processing.
2. Analyzing the images to develop plots from which the fractal dimension could be deduced.
3. Performing the required analyses to quantify the fractal dimension of the soil microstructure.

This report summarizes the results of this portion of the Phase II results.

## PRINCIPLES OF FRACTAL GEOMETRY

The fundamental principles of fractal geometry were described by Mandelbrot (Ref. 2), and a modern exposition on these principles has been presented by Peitgen, et al. (Ref. 3). For purposes of this research, it was desired to determine the fractal dimension of soil microstructure as opposed to the fractal dimension of individual soil grains. In this regard, the description of soil microstructure is taken to be the description of the way in which individual soil grains interact with each other as reflected in their interconnectivity. This interpretation seems appropriate in that one of the fundamental factors influencing the strength and compressibility of soils is the quasi-structural arrangement formed by interconnected particles touching in space to form a framework with quantifiable rigidity.

The specific implementation of these concepts requires that the fractal properties of the spatial arrangement of multi-particle clusters be measured. The applicable analytical principle drawn from fractal geometry is that the fractal dimension of a cluster of geometric shapes can be determined by taking the slope of a plot of logarithm of cluster area versus logarithm of cluster perimeter. Algebraically this becomes

$$\log(A) = \frac{D}{2} \log(P) + C \quad (1)$$

where D is the fractal dimension

A is cluster cross sectional area

P is cluster perimeter, and

C is an intercept.

Traditionally, it has been presumed that the direct measurement of cluster area and perimeter would be overly laborious, thus other, less arduous, analytical techniques have been devised (c.f. Voss, Ref. 3) involving overlaying squares on bit-mapped raster images of clusters. However, our computer analysis techniques were capable of yielding direct measurements of both particle area and particle perimeter so that the more accurate mathematical technique described by Equation 1 could be employed.

#### DATA ACQUISITION TECHNIQUES

The desire was to obtain images of soil samples showing clusters formed by interconnected sand particles whose area and perimeter could be measured. It was decided that the best images could be obtained if intermediate steps such as photographic negatives and/or prints could be avoided insofar as possible. To accomplish this, a technique was developed to directly scan images of soil samples within the 10 to 100 mesh size range.

The sand samples were deposited directly onto a glass microscope cover slide and held there with a clear cement. The glass cover slide was a 22mm by 30mm cover slide supplied by Fisher Scientific Company (Cat. No. 12-545A). These slides are manufactured to possess a high degree of optical clarity because specimens are normally viewed through these slides in a microscope.

The cement employed was prepared by cutting one part of clear high-gloss brushing lacquer with 2 parts of clear lacquer thinner. The liquid was spread in a thin layer onto the slide, and sand was sprinkled or sieved onto the slide until a sufficient density was obtained to yield a number of clusters of finite size separated by individual sand particles and void space. When the lacquer dried, the sand was held sufficiently strongly to the slide so that the slide could be turned upright for analysis.

The slide was then inserted into a Howtek Scanmaster 35 II scanner. This scanner is designed to scan 35mm photographic slides at a resolution of 3000 dots per inch. The scanner is capable of three modes of operation: (1) binary threshold scanning, (2) 8 bit (256 shades of gray) gray scale scanning, and (3) 24 bit, three raster red, green, blue (256 color) color scanning. The mode selected was the 256 gray scale mode because this would allow more careful selection of an appropriate gray scale threshold value during subsequent processing.

The images thus obtained were extremely sharp, and edge detection (originally thought to be a challenge) was in fact, trivial. Because of the uniform clarity of the glass slide and lacquer, it was found that the background gray level could be thresholded at a single gray scale level. In fact, virtually the entire background was at a single gray scale value. This resulted in an image having exceptionally robust analytical potential and displaying very few experimental artifacts.

#### DATA REDUCTION

The steps in data reduction consisted of (1) thresholding the 8 bit gray scale image into a binary image, (2) using a paint program to remove artifacts, (3) vectorizing the clusters into polygons, (4) determining the area and perimeter for the polygon associated with each cluster, and (5) writing the data to a database file for subsequent analysis.

The software used to accomplish this was the Map and Image Processing System (MIPS) developed and distributed by MicroImages, Inc., 201 North 8th Street, Suite 15, Lincoln, Nebraska, 68508-1347. This system is an exceptionally versatile Geographic Information System (GIS) whose standard features provided all of the analytical capabilities required for this project. Analysis was performed on a 20 MHz 386 AT bus microcomputer with math coprocessor. A 338 MegaByte hard disk was employed because of the data-intensive nature of the research.

The exact menu sequences employed in the analysis are described in detail in Appendix A. In the following discussion, the focus is on the analytical principles employed.

The first step in the analysis was to perform an 8 bit (256 level) grayscale scan (see Figure 1). Next, this image was converted into a 2 bit binary (black and white) image. It was necessary to select a threshold value of gray from among the 256 shades displayed. MIPS examination features allowed for selecting a particular gray shade and highlighting all pixels having that shade of gray in a false color. One would then hope that the voids portion of the image would exhibit gray scale at and/or below the threshold level and that the soil clusters would display gray scales above the chosen threshold level. Of course, this was not uniformly the case. Nevertheless, the voids exhibited gray scale levels not only at and/or below the threshold level, but in most cases displayed a single value at the threshold level. This was a result of the exceptional clarity of the glass slide/lacquer combination.

The principal difficulty encountered was that the interior portions of the sand particles sometimes exhibited gray tones within the range otherwise devoted to the voids. This occurred due to light reflecting off of the curved particle surfaces. Therefore, for the second step in the analysis, these obvious artifacts were removed using the paint capabilities of the MIPS software. This process could have been done automatically by MIPS; however, not all white areas within black areas were artifacts. Some white areas were caused by true voids showing through where three or more sand particles came in contact.

Figure 2(a) shows some of these artifacts, and Figure 2(b) shows the result after manual painting. For most samples, the manual painting took only a few minutes; however, in some cases the process took up to one-half hour. It should be noted, however, that a typical slide contained around 1000 clusters.

Occasionally, air bubbles or dust particles needed to be manually painted out of the voids areas of the images. In addition, fiduciary marks were inked on the slide edges to allow setting the size scale for the analysis within MIPS. These fiduciary marks were also manually painted out of the images after the image scale had been set.

The third step in the data reduction was to vectorize the thresholded images. MIPS accomplished this automatically. The vectorized cluster polygons were stored in a separate disk file for further analysis. It is important to note that there were two different types of polygons vectorized. Class 1 polygons were "islands" within clusters and were formed by voids showing through near the contacts among multiple particles. (These were the features that were not "painted out" in the previous analysis step.) Class 2 polygons were the sand clusters themselves. Fortunately, MIPS has the intelligence to distinguish between these two types of polygons and to assign them different Class Numbers in the vector file.

The fourth step in the data reduction was to calculate the areas and perimeters of the polygons representing the sand clusters. MIPS performed these calculations automatically. It was necessary to instruct the software that the Class 2 polygons were the only

ones desired. MIPS then calculated the areas and perimeters. MIPS was capable of subtracting off the areas of any islands that existing within clusters due to void space showing through at contacts between several particles. Additionally, MIPS could calculate cluster perimeters with the perimeter due to such islands added in. MIPS also calculated a roughness factor defined as:

$$\text{ROUGHNESS} = \frac{D_{\text{max}} \times L_{\text{max}}}{A_{\text{min}}} \quad (2)$$

where  $D_{\text{max}}$  = maximum diameter across cluster  
 $L_{\text{max}}$  = boundary length including boundaries around islands  
 $A_{\text{min}}$  = cluster area excluding islands.

As a fifth step in the analysis, the results were written to a database file. The desired entries in the database file were the "area minus islands" which was the area of the cluster less the area occupied by any included Class 1 polygons (voids), the "perimeter plus islands" which was the external perimeter of the sand polygons plus the perimeter of any included islands (voids), and the roughness. The capability of MIPS to recognize and quantify these cluster/void interrelationships was essential to the efficient analysis of the data.

The data thus stored was in a form that it could be imported into any standard spreadsheet for plotting and further analysis. In particular, LOTUS Symphony was used for this project.

## VERBAL DESCRIPTION OF SAMPLES TESTED

Tests were performed on 31 samples of 6 different sands:

UR SAMPLES: This material was a standard Ottawa research sand.

All material used passed the 20 mesh size, and the master sample was split into fractions for preparation of individual samples:

Slide UR1 was composed of material in the 20 to 40 mesh size range. Slide UR2, UR4, and UR5 were composed of material in the 20 to 60 mesh size range. The slides differed in that there were different densities of material on each slide. The slides in order of increasing density were UR4, UR5, and UR2. Slide UR3 was composed of the unsieved sample.

WGA SAMPLES: This material was a washed commercial sand. The larger particles are rounded. Two slides, WGA1 and WGA2, were prepared from the same source material; however, the density of the material on slide WGA2 was greater than that on slide WGA1.

WGR SAMPLES: This material was a standard research sand. The sample was composed of material passing the 40 sieve. Three samples WGR2 through WGR4 prepared from same source material but with differing densities of sand the on slides. The slides, in order of increasing density of material, are WGR4, WGR2, and WGR3.

UA SAMPLES: This material was a crushed feldspar sand. UA2, UA3, and UA4 are composed of material in the 20 to 40 sieve size range. UA5 and UA6 are composed of the unsieved sample on slides.

Finally, a series of 12 similar slides was prepared from material between the 40 and 60 mesh size for a sample called UABULK. The combined data from these samples yielded over 8000 data points.

AL SAMPLES: This material was an angular crushed limestone.

Samples AL1, AL2, and AL3 are in the 20 to 60 mesh size range.

All samples were deposited on the slides at approximately the same density.

GILL SAMPLES: These samples were a well rounded uniform sand supplied by the Air Force as representative of materials being used in other research. A single sample, GILL, was tested.

## PICTORIAL AND QUANTITATIVE DESCRIPTION OF SAMPLES TESTED

### THRESHOLDED IMAGERY

Perhaps the best description of the individual samples can be given by showing the thresholded images obtained during the image processing as shown in Figures 3 through 22.

### PARTICLE SIZE DISTRIBUTIONS

The particle size distributions of the particles on the slides were determined by extracting the areas of the small clusters. The small cluster were defined as those clusters that had an area less than that of the typical particle for the sample. This threshold particle size was determined by selecting individual particles from the thresholded image. The particle size distribution curve is presented in Figures 23a through 35a as plots of the cumulative distribution function for the individual particles.

### PARTICLE ROUGHNESS

The particles were further characterized by the distribution functions for the roughness values determined on the small clusters, presuming that small clusters were composed predominantly of individual particles. Histograms of probability for small cluster roughness are shown in Figures 23b through 35b.

## PRINCIPLES OF FRACTAL DATA ANALYSIS

It was previously shown (Eq. 1) that the principle upon which the experimental determination of fractal dimension is based is the determination of the slope of a full log plot of cluster perimeter versus cluster area. A typical plot is shown in figure 36.

The large amount of soil cluster data obtained presented analysis challenges beyond those encountered in previous studies where relatively few data points were collected. In particular, reference to figure 49 shows that there appears to be considerable scatter in the data; however, what appears to be scatter cannot be attributed to experimental error. Rather, the scatter represents a true dispersion of cluster geometry for the numerous clusters measured. Thus, while the idea of a best statistical fit to the data could have been implemented, such an approach would have resulted in the loss of real information rather than resulting in the averaging out of errors.

### ANALYTICAL CONSIDERATIONS FOR TWO OVERLAPPING CIRCULAR SPOTS

Consider, for example, a cluster composed of two circular spots of equal radius having varying degrees of overlap. It is possible to measure the area and perimeter of such clusters and to develop a mathematical expression for both area and perimeter as a function of spot overlap. The required geometry is shown in figure 37(a), and the mathematical derivations are given in Appendix B. This geometric configuration gives rise to the following expressions:

$$A = 2r^2 + 2ar^2 - a^2 - 2r^2 \arcsin(-a/r) - r^2 \quad (3)$$

$$P = 4r[1 - \arccos(a/r)] \quad (4)$$

where  $A$  = cluster area

$P$  = cluster perimeter

$a$  = distance to symmetry point

$r$  = spot radius

If  $a = 0$  then the two spots overlap completely; if  $a = r$  the two spots are just tangent to each other; and if  $a > r$  the two spots are separated.

Figure 37(b) shows a plot of  $\log(\text{Area})$  versus  $\log(\text{Perimeter})$  for the above expressions using four values of spot radius. The solid data points are for a series of four spots with  $a > r$ ; (i.e. the spots are separated), and for varying spot radius,  $r$ . As expected, these points lie in a straight line with a slope of  $1/2$  implying a fractal dimension of 1 as would be expected for spots that do not interact or overlap in any way.

The half solid data points are for configurations where two spots are just tangent to each other. By this is meant that the spots are touching such that they are viewed as a single cluster, but virtually the full two-spot area and two-spot perimeter are developed. From a general perspective, such tangent spot pairs also represent a uniquely defined geometry, thus lines connecting the half solid points also display a slope of  $1/2$  implying a fractal dimension of 1.

Connecting the solid data points with their respective half solid

data points results in a fractal dimension reflecting full spacing-filling potential. Thus, lines connecting these point pairs have a slope of 1, implying a fractal dimension of 2. This is the value that would be expected for a space-filling geometry.

The open data points represent varying degrees of overlap for two spots having the same radius as the spots of the solid data points and of the half solid data points. Note that these points plot along curved loci having slopes that always exceed 0.5.

#### ANALYTICAL CONSIDERATIONS FOR TWO OVERLAPPING SQUARES

As a second example, consider squares that are oriented with their sides parallel to each other. Two such squares can overlap completely to form a single square, or can be separated incrementally to form rectangles. In the limit, two squares can be just tangent to each other so that they share a common side. In this case, the common side contributes nothing to the perimeter of the cluster. With an infinitesimally small additional separation, the squares become two independent squares with individual sides where the pair almost meet.

The required geometry is shown in figure 38(a), and the mathematical derivations are given in Appendix B. This geometric configuration gives rise to the following expressions:

$$A = 4r^2 + 4ar \quad (5)$$

$$P = 8r + 4a \quad \text{for } a < r \quad (6a)$$

$$P = 16r \quad \text{for } a > r. \quad (6b)$$

where  $A$  = cluster area

$P$  = cluster perimeter

$a$  = distance to symmetry point

$r$  = half side length of square

If  $a = 0$  then the two squares overlap completely; if  $a = r$  the two squares are just tangent to each other; and if  $a > r$  the two squares are separated.

Figure 38(b) shows a plot of  $\log(\text{Area})$  versus  $\log(\text{Perimeter})$  for the above expressions. The solid data points are for a series of squares with  $a > r$ ; (i.e. the squares are separated), and for varying length of side,  $2r$ . As expected, these points lie in a straight line with a slope of  $1/2$  implying a fractal dimension of 1, as would be expected for squares that do not interact or overlap in any way.

The half solid data points are for configurations where two squares are just tangent to each other. By this is meant that the squares are touching such that they are viewed as a single cluster, but the full two-square area remains. However, the two-square perimeter is not developed because the squares share a common side. The side length for each of the two squares in this pair is equal, and is equal to the side length for the solid data points. Thus lines connecting the solid data points with their respective half solid data point has a slope of 1, implying a fractal dimension of 2. This is the value that would be expected for this space-filling geometry.

The open data points represent the results of varying degrees of

overlap for two squares having the same side length as the squares of the solid data points and of the half solid data points. Note that these points plot along slightly curved loci having slopes that always exceed 0.5.

#### ANALYTICAL CONSIDERATIONS FOR TWO OVERLAPPING DIAMONDS

As a final example, consider squares that are oriented with their sides at 45 degrees to the horizontal (i.e. rectilinear, equal-sided diamonds). Two such diamonds can overlap completely to form a single diamond, or can be separated incrementally. In the limit, two diamonds can be just tangent to each other so that they touch at points. With an infinitesimally small additional separation, they become two independent diamonds.

The required geometry is shown in figure 39(a), and the mathematical derivations are given in Appendix B. This geometric configuration gives rise to the following expressions:

$$A = 2r^2 + 4ar - 2a^2 \quad (7)$$

$$P = 2(r + a) \quad (8)$$

where  $A$  = cluster area

$P$  = cluster perimeter

$a$  = distance to symmetry point

$r$  = half side length of square

If  $a = 0$  then the two diamonds overlap completely; if  $a = r$  the two diamonds are just tangent to each other; and if  $a > r$  the two diamonds are separated.

Figure 39(b) shows a plot of  $\log(\text{Area})$  versus  $\log(\text{Perimeter})$  for the above expressions. The solid data points are for a series of diamonds with  $a > r$ ; (i.e. the diamonds are separated), and for varying length of side. As expected, these points lie in a straight line with a slope of  $1/2$  implying a fractal dimension of 1, as would be expected for diamonds that do not interact or overlap in any way.

The half solid data points are for configurations where two diamonds are just tangent to each other, i.e. the diamonds are touching such that they are viewed as a single cluster, but the full two-diamond area is developed. The side length for each of the two diamonds in this pair is equal, and is equal to the side length for the solid data points. Thus lines connecting the solid data points with their respective half solid data point has a slope of 1, implying a fractal dimension of 2. This is the value that would be expected for this space-filling geometry.

The open data points represent the results of varying degrees of overlap for two diamonds having the same side length as the diamonds of the solid data points and of the half solid data points. Note that these points plot along curved loci having slopes that always exceed 0.5.

#### COMPARISON OF ANALYTICAL RESULTS

It is interesting to compare the analytical results for the various shapes, all of which have the same value for area. Figure

40 shows the results superimposed for an area of 100. The circular data points are for the spot particles, the square data points are for the squares, and the diamond shaped points are for the diamonds. Note that the areas for all three cases are the same for complete overlap and for zero overlap. This is because the basic shapes were selected so that they had the same areas. For complete overlap, the spot data points lie below the square and diamond points because a circle displays the least area of any geometric shape for a given perimeter. For complete overlap, the square and diamond data points are identical because the basic shape is square whether or not it is rotated.

As the particles diverge from complete overlap, the difference in behavior of the shapes is apparent. It is particularly interesting to compare the squares and diamonds. These geometric shapes are, of course, identical except for the rotation involved. Yet, the behavior of the data points on the plot is radically different. The squares show a relatively linear behavior and abruptly jump up just as the particles separate. This is because of the sudden increase in perimeter just as the two particles separate. The diamond spaced particles, however, display a smoothly curved transition as the particles diverge from complete overlap, and there is no abrupt jump in perimeter value as the particles separate because the perimeter of the separating diamonds develops gradually. Clearly, if a simple act of rotating identical particles can result in radical differences in the appearance of the  $\text{Log}(A)$  versus  $\text{Log}(P)$  plot, there is little likelihood that a simple analytical relationship exists that would predict how the fractal dimension changes as the relative positions of a variety of irregularly-shaped particles of varying

size interact.

The above argument demonstrates why the experimental data (c.f. figure 36) shows the dispersion that it does. It also explains why there are apparent lower bounds to the data, with data extending in a somewhat disordered manner above the lower bound.

As a lower bound, one would consider a suite of circular particles because they will always show the smallest perimeter to area ratio and will therefore plot at the lowest possible value of  $\text{Log}(P)$  for a given value of  $\text{Log}(A)$  on a  $\text{Log}(A)$  versus  $\text{Log}(P)$  plot. In fact, an analytical expression can be derived for this lower bound based on equations (7) and (8):

$$\log(P) = \frac{1}{2} \log(4) + \frac{1}{2} \log(A) \quad (9)$$

Note that Equation (9) gives a slope of .5 corresponding to a fractal dimension of one.

While a theoretical lower bound exists on this relationship, there is no theoretical upper bound. This is because as particles become more needle like, the perimeter increases without bound whereas the area approaches zero.

As particles touch to form clusters, it is also possible to determine an approximate upper bound at which the  $\text{Log}(A)$  versus  $\text{Log}(P)$  curve undergoes a transition to a slope of 1 (fractal dimension of 2). This bound is imposed by the physical nature of the problem studied because each sample studied has a maximum particle size. Thus clusters composed of more than one of these

largest particles represent an upper limit at which the  $\text{Log}(A)$  versus  $\text{Log}(P)$  curve will assume a slope of 1 corresponding to a fractal dimension of 2.

In conclusion, one would expect data points to lie above a lower bound pair of lines given by (1) the equation of circular spots at lower areas, and (2) line line having a slope of 1 and departing from the theoretical circular relationship at a value of area corresponding approximately to the largest particle area represented in the sample examined.

#### RECOMMENDED ANALYSIS PROCEDURE

The conclusion that can be drawn from the above analysis is that there is no analytical approach to suggest a simple geometric form that should be displayed for a fractal plot in the transition region between the region where particles act as individuals and the region where they act as space filling clusters. Therefore, there is no simple analytical model that could serve as a basis for developing a smoothing function that could be used to fit a line to experimental data. In particular, the concept of a least squares fit of a line to data has no basis in theory, even though it could be used as a practical expedient.

Indeed, ample analytical evidence is presented in the above paragraphs to substantiate the need for a truly innovative analytical approach based on functions that are not single valued but are capable of exhibiting results which are dispersed in a controlled manner above a pair of lower bounds on a  $\text{Log}(A)$  versus  $\text{Log}(P)$  plot. Developing such mathematical techniques would be a

complicated process, and their development is beyond the scope of this research.

It appears that the most appropriate approach to data analysis for this research is to determine the slope of the fractal plot in the transition region either by eye or by a least squares fit. The least squares fit approach is limited because there is no basis for assuming linearity in the transition region. Neither is there any analytical function for the transition that could serve as a basis for a non-linear least squares fit. Thus, the most appropriate approach appears to be to fit the relationships by eye. When this approach was applied to the large amount of data available in this study, there was never a problem in selecting a best fit line through the data by eye.

#### ANALYSIS OF THE EXPERIMENTAL DATA

The basic approach to analyzing the fractal properties of the data was to plot log of area versus log of perimeter. The data for the test results was robust in that the plots for the various samples examined contained from 100 to as many as 8000 data points. To the author's knowledge, no previous fractal studies have been based on so rich a data base. Moreover, because direct scanning and vectorization of images was used, the data are of a significantly higher quality than most obtained previously for real natural features.

The results of plots of log of area versus log of perimeter are shown in figures 41 through 53. Typically, these plots show a

region at small areas (and perimeters) where the best fit straight line has a slope of .5, giving a fractal dimension of 1. This is as expected for single particles acting independently. The plot then shows a transition region with a slope of between .5 and 1.0 implying a fractal dimension between 1 and 2. This is the region where clusters are forming, and the material is going through a transition to a space-filling character. As discussed in section 6, the slope in the transition region was determined by eye. Finally, in the larger area (perimeter) portion of the plot, the slope approaches 1, implying a fractal dimension of 2. This portion of the curve was typically not well defined by the data because the slides were prepared in a manner that promoted small to medium sized clusters, there being no point in preparing slides that were virtually completely filled with a few very large clusters of particles.

Table 1 presents the final values determined for the fractal dimension of the samples tested. In addition, average cluster roughness determined from the data shown in figures 23b through 35b are also tabulated.

TABLE 1. Summary of data.

| Sample    | Average Small Cluster Roughness | Fractal Dimension |            |
|-----------|---------------------------------|-------------------|------------|
|           |                                 | Least Squares     | Fit By Eye |
| UR1       | 6.72                            | 1.69              | 1.6        |
| UR2, 4, 5 | 7.02                            | 1.66              | 1.6        |
| UR3       | 7.73                            | 1.59              | 1.6        |
| WGA1      | 7.57                            | 1.60              | 1.9        |
| WGA2      | 7.45                            | 1.60              | 1.9        |
| WGR2      | 8.28                            | 1.63              | 1.8        |
| WGR3      | 7.97                            | 1.55              | 1.6        |
| WGR4      | 8.81                            | 1.66              | 1.5        |
| UA2, 3, 4 | 7.84                            | 1.71              | 1.8        |
| UA5, 6    | 7.69                            | 1.69              | 1.6        |
| UABULK    | 8.86                            | 1.80              | 1.7        |
| ALL, 2, 3 | 8.16                            | 1.40              | 1.5        |
| GILL 6    | 8.17                            | 1.84              | 1.9        |

## RESULTS

The study clearly demonstrates that there are measurable differences in the fractal dimension representing particle interconnectivity in sands. The measured values range from 1.5 to 1.9. The possible range is, of course, 1.0 to 2.0. Thus, given the extremes possible, the data from the 6 different sands spans 40% of the possible range. Therefore it can be concluded that the approach to analysis is viable in that there is a substantial variation from soil to soil for the void ratios studied.

What is less clear is the relationship that these measured values have to the strength and compressibility of the soils. This is because there were no strength determinations performed on the samples. Nevertheless, it is possible to obtain some measures that might demonstrate whether or not there is a relationship

between fractal dimension and strength and/or compressibility.

#### SMALL PARTICLE ROUGHNESS

One of the measures used to characterize the samples tested was small cluster roughness as defined by Equation (2), repeated here for ease of reference.

$$\text{ROUGHNESS} = \frac{D_{\max} \times L_{\max}}{A_{\min}} \quad (2)$$

where  $D_{\max}$  = maximum diameter across cluster

$L_{\max}$  = boundary length including boundaries around islands

$A_{\min}$  = cluster area excluding islands.

Recall that small clusters were clusters whose areas were small enough to reasonably assure that the clusters consisted of individual sand grains. Therefore, the small cluster roughness thus defined and measured could reasonably be expected to be a measure of the roughness of the individual soil grains. Figure 54 plots fractal dimension versus average small cluster roughness. There appears to be a trend for decreasing fractal dimension with particle increasing roughness.

It is not obvious how this relationship can be interpreted because roughness is a composite parameter involving particle elongation, particle perimeter, and particle area. Nevertheless, for the sands tested, the particles were on the whole bulky rather than elongated. Therefore, it can be reasonably assumed that the ratio of maximum diameter across cluster ( $D_{max}$ ) to cluster area excluding islands ( $A_{min}$ ) is relatively constant. It appears likely that the most important factor influencing the roughness is the boundary length including boundaries around islands ( $L_{max}$ ). This, in turn, is a measure of the jaggedness (roughness) of the surface of the sand particles. If this be the case, the results demonstrate that the space-filling tendency of the aggregated clusters (as reflected in the fractal dimension) decreases with the jaggedness of the particle surfaces. This would be consistent with stating that the higher the jaggedness of the surface of the particles the less space filling the soil microstructure. This is consistent with other observations regarding soil microstructure.

#### CONCLUSIONS

It can be concluded that the fractal analysis employed in this research can be used to quantitatively relate fractal dimension to soil structure. Moreover, for the soil studied, there is a definable relationship showing increasing openness of soil microstructure with increasing roughness of the individual soil particles.

## RECOMMENDATIONS FOR PHASE III WORK

The recommended Phase III research program is as follows:

- (1) Perform additional test on samples were there is laboratory test data relating to the strength and compressibility of the soils tested.
- (2) Perform additional mathematical analyses designed to investigate possible advanced data analysis techniques for extracting a fractal dimension from  $\log(A)$  versus  $\log(P)$  curves. These techniques should incorporate consideration of the analytical work presented in the section entitled PRINCIPLES OF FRACTAL DATA ANALYSIS.
- (3) Extend the analysis principles presented herein to data obtained on samples that have been subjected to known loading scenarios.
- (4) Implement the principles described herein in a three-dimensional context.

#### REFERENCES

1. Krepfl, M., Moore, C. A., and Lee, W. E., "A Quantitative Description of Soil Microstructure Using Fractals, Volume I - Research Results," Final Report, U. S. Air Force Contract F29601-88-C-0058, Geotechnics, Inc., January, 1989.
2. Mandelbrot, B. P., The Fractal Geometry of Nature, W. H. Freeman and Co., New York, 1983.
3. Peitgen, H.-O., and Saupe, D., eds., The Science of Fractal Images, Springer-Verlag, New York, 1988.

## APPENDIX A

### PROCEDURE FOR IMAGE ACQUISITION AND ANALYSIS

- Step 1a - Start computer.
- Step 2 - Enter MIPS to invoke software.
- Step 3 - Turn on Howtek 35 II scanner.
- Step 4a - Set parameters and calibrate scanner by invoking  
PREPARE/SCAN/SCANMSTR 35/PARAMETERS/.
- Step 4b - Click on the following buttons: RESOLUTION (3000), INPUT  
TYPE (B/W), CONTRAST (Linear), ENHANCEMENT (None).
- Step 4c- Then click on SPECIAL (Calibrate).
- Step 4d - Place dark card in scanner as requested.
- Step 4e - Remove dark card and reinsert carrier for light  
calibration.
- Step 5 - Mount slide to be analyzed on 35mm film carrier and  
insert in scanner.
- Step 6 - Enlarge scanning window to include entire area that  
scanner is capable of covering.
- Step 7 - Click on SCAN (Fast Preview).
- Step 8 - Reduce scanning window to include desired portion of  
slide for analysis.
- Step 9a - Click on SCAN (To File).
- Step 9b - Click on RVF Single Raster.
- Step 9c - Click on Start Scan.
- Step 10a - Respond to query with Upright (U) Rotation.
- Step 10b - Use standard file selection procedure to select a file  
within which to place the image.
- Step 10c - Wait for image to be scanned.
- Step 11a - Double click on mouse to move out of scan mode.
- Step 11b - Press F1 twice to back up to main MIPS menu.

- Step 12 - Select DISPLAY/RASTER from main menu.
- Step 13 - Click on New Rast(s).
- Step 14 - Use standard select procedure to select the greyscale image created in Step 10c.
- Step 15 - Click on following button on display menu: SELECT (Single Raster), ERASE (Screen), DESTINATION (Full Screen), OVERLAY (None), SPECIAL (Gray Scale).
- Step 16 - Click on ACTIONS (Redisplay) to display image.
- Step 17 - Click on SPECIAL (Edit Colors).
- Step 18 - Click on ADJUST in COLOR PALLETTE window.
- Step 19 - Click on a carefully selected area of interest on the image. The goal here is to find an area that will allow you to select a gray scale level to distinguish between particles and background.
- Step 20 - Click on a representative background area in the microscope window of the COLOR PALLETTE. This will typically select a gray scale of around 251 (with 255 being pure white).
- Step 21 - Click on the right mouse button to Flash Current. This will cause all pixels with the selected value (e.g. 251) to be highlighted in a bright red color. In the event that the background is banded over more than one grayscale value, select the lowest value. Record the value of this background level for later use.

- Step 22 - Double click mouse twice and press F1 once to back up to main MIPS menu.
- Step 23 - Select INTERPRET/COMBINE/LOGICAL/THRESHOLD.
- Step 24a - Respond to query with white Above Threshold.
- Step 24b - Use the standard select procedure to select the greyscale image created in Step 10c.
- Step 24c - Respond to the query with the Threshold Value determined in Step 21.
- Step 25 - Use the standard select procedure to select a new raster to hold the thresholded image.
- Step 26 - Wait for new raster to be created. MIPS will threshold the gray scale image to create a new binary black and white image with the particles shown in black and the background shown in white.
- Step 27 - Press F1 three times to back up to MIPS main menu.
- Step 28a - Select DISPLAY/RASTER/SINGLE.
- Step 28b - Use the standard select procedure to select the thresholded image created in Step 26.
- Step 29 - Click on the following options in the DISPLAY RASTER window: SELECT (Single Raster), ERASE (Screen), DESTINATION (Full Screen), OVERLAY (None).
- Step 30 - Click on ACTION (Redisplay) to display thresholded image.
- Step 31a - Click on ACTION (Change View).
- Step 31b - Press F8 to Zoom Out so that the entire image can be seen. In particular, it is desired to see the fiduciary marks scribed on the edges of the slide.
- Step 32 - Double click twice on the mouse to back out to MIPS Main Menu.

- Step 33a - Press F4 Measure.
- Step 33b - Click on ALIBRATE in the MEASURE window.
- Step 33c - Slide the two horizontal calibrate bars up and/or down until they coincide with the fiduciary marks on the slide.
- Step 33d - Press F6 VCal for vertical calibration.
- Step 33e - Respond to query with .00022 for a distance of 22mm.
- Step 33f - Respond to query for Save Cell Size Calibration with Rasters with Yes.
- Step 33g - Use the standard selection procedure to select the threshold image to save the calibration to.
- Step 34 - Press F2 SavC to save calibration.
- Step 35 - Double click the mouse twice to back up to the MIPS Main Menu.
- Step 36a - Select PREPARE/RASTER/EDIT-RASTER.
- Step 36b - Use the standard selection procedure to select the thresholded image.
- Step 36c - Respond to Edit Raster inPlace query with Yes.
- Step 36d - Respond to Warning -Changes are Permanent query with Yes.
- Step 36e - Click on right mouse button to use selected area.
- Step 37 - Click on PAINT in DRAW TOOLS window. Paint out any artifacts in the image. These might include (1) fiduciary marks, (2) tape or slide holder at slide edges, or (3) white spots in the interior of particles resulting from reflected light. Save image back into file that held original threshold image when done. (Optionally, create a new cleaned threshold image.) There are several "hot key" options that will greatly expedite the cleaning process.

- Step 38 - Double click on mouse once and press F1 twice to back up to MIPS Main Menu.
- Step 39a - Select PREPARE/RAST->VECT/AUTO-BOUNDS.
- Step 39b - Use the standard selection procedure to select the cleaned thresholded image.
- Step 39c - Respond to the query about output object type with V for Vector object.
- Step 39d - Use the standard selection procedure to select a new vector object to hold the vectorized image.
- Step 39e - Respond Yes to query about echoing lines to the screen.
- Step 39f - Respond No to the query about cutting corners.
- Step 39g - Wait for MIPS to vectorize the image. This will create polygons delineating the particle clusters. There will also be island polygons where the background shows through the particle clusters near contacts between individual particles. The island polygons will be given a different type number by MIPS than the cluster polygons.
- Step 40 - Press F1 twice to back up to MIPS Main Menu.
- Step 41 - Select INTERPRET/VECTOR/POLYGON.
- Step 42 - Respond None to query about overlaying vector on another image.
- Step 43 - Use the standard selection procedure to select the image as vectorized in Step 39g.
- Step 44 - Respond No to query about setting the scale of the image.
- Step 45 - Use standard selection procedure to set destination file for output from process.
- Step 46 - Respond No to query to output text file description records.

- Step 47a - Press F8 Menu to determine polygons to select.
- Step 47b - Respond to properties query with Class.
- Step 47c - Select WHITE as the class. (Note: You must not only move the pointer down to WHITE, you must also move the pointer into WHITE.)
- Step 47d - Wait for the process to finish. You can monitor the progress by observing the polygons as they are processed on the display screen.
- Step 48 - Double click the mouse and press F1 twice to back up to the MIPS Main Menu.
- Step 49 - Confirm that a filename.TXT file was generated containing the results of the analysis. This file contains the following information: polygon number, perimeter, polygon perimeter plus perimeter of any included islands (one of the parameters used for fractal analysis), area, area less any islands (the other parameter used for fractal analysis), area/perimeter ratio, AreaPerI, roughness [maximum (diameter x boundary length ignoring islands)/ area ignoring islands], X distance to centroid, Y distance to centroid, Data X, Data Y, Label X, Label Y, Ref #, Group, and Class. There is one set of entries in the data base for each polygon analyzed.
- Step 50 - The .TXT file is an ASCII file, and can be imported into any database software for further analysis. For this research, LOTUS Symphony was the software package use. The details of the import process are not described here because they are well documented in any database software package and differ from package to package. The essence of the analysis is to import particle

perimeter plus islands and particle area minus islands  
and then plot log of perimeter versus log of area. The  
slope of such a plot is twice the fractal dimension.

- Figure 23a. Particle size distribution for sample UR1.
- Figure 23b. Histogram of probability of particle roughness for sample UR1.
- Figure 24a. Particle size distribution for sample UR2, 4, 5.
- Figure 24b. Histogram of probability of particle roughness for sample UR2, 4, 5.
- Figure 25a. Particle size distribution for sample UR3.
- Figure 25b. Histogram of probability of particle roughness for sample UR3.
- Figure 26a. Particle size distribution for sample WGA1.
- Figure 26b. Histogram of probability of particle roughness for sample WGA1.
- Figure 27a. Particle size distribution for sample WGA2.
- Figure 27b. Histogram of probability of particle roughness for sample WGA2.
- Figure 28a. Particle size distribution for sample WGR2.
- Figure 28b. Histogram of probability of particle roughness for sample WGR2.
- Figure 29a. Particle size distribution for sample WGR3.
- Figure 29b. Histogram of probability of particle roughness for sample WGR3.
- Figure 30a. Particle size distribution for sample WGR4.
- Figure 30b. Histogram of probability of particle roughness for sample WGR4.
- Figure 31a. Particle size distribution for sample UA2, 3, 4.
- Figure 31b. Histogram of probability of particle roughness for sample UA2, 3, 4.
- Figure 32a. Particle size distribution for sample UA5, 6.
- Figure 32b. Histogram of probability of particle roughness for sample UA5, 6.
- Figure 33a. Particle size distribution for sample UABULK.
- Figure 33b. Histogram of probability of particle roughness for sample UABULK.
- Figure 34a. Particle size distribution for sample AL1, 2, 3.
- Figure 34b. Histogram of probability of particle roughness

for sample AL1, 2, 3.

Figure 35a. Particle size distribution for sample GILL.

Figure 35b. Histogram of probability of particle roughness  
for sample GILL.

## NODE NUMBERING SCHEME

This appendix is intended to demonstrate the node numbering scheme and to show typical input for an example problem. The level 0 mesh consists of one triangular element and three nodal points, the level 1 mesh consists of 4 triangular elements and 6 nodal points. The order in which the elements and nodal points for a particular level are identified is shown for levels 0 through 3 in figure B1. Higher levels would follow the same procedure; i.e., the nodal points are sequentially numbered from 1 starting at the upper tip of the triangle and proceeding down to the left and right until all of the nodal points are identified.

The elements are identified in a routine manner wherein the first element has the nodal points (1, 2, 3) in a counterclockwise connectivity numbering scheme. The next elements follow below element number 1 along the left hand side of the outmost triangle; i.e., the level 0 boundaries, until the last element which would be the triangular element in the bottom left-hand side. The next elements are numbered starting from the element below element 1 to the right, following according to figure B1. This numbering sequence is continued until the bottom right-hand most element is identified. Remaining elements are then numbered as shown in figure B1.

The numbering scheme results in all of the right-side-up triangles being numbered first in a predictable scheme, and then the

upside-down triangles are numbered.

Table B1 gives the number of elements and nodal points for the first 7 mesh generation levels.

TABLE B1. Elements and nodal points for mesh levels.

| LEVEL | NO. ELEMENTS | NO. NODAL POINTS |
|-------|--------------|------------------|
| 0     | 1            | 3                |
| 1     | 4            | 6                |
| 2     | 16           | 15               |
| 3     | 64           | 45               |
| 4     | 256          | 153              |
| 5     | 1024         | 561              |
| 6     | 4096         | 2145             |
| 7     | 16384        | 8385             |

#### INPUT DATA

The main program calls for seven items to be read in: HEAD, PROB, LEVEL, LTYPE, NMAT, NPC, and NUMBC. Each is discussed separately below.

#### HEAD

This card is used to input the user-selected title of the problem.

#### PROB

The program can perform either a static or a dynamic analysis. A static analysis is specified by a 1 input, and a dynamic analysis is specified by a 2 input.

#### NMAT

NMAT is the number of different types of materials to be specified. NMAT must assume a value of 1 more than the level of the mesh generation. For example, if LEVEL = 0 then NMAT = 1.

#### NPC

This defines the total number of pressure input cards; i.e., the number of nodes over which a uniform load is assumed to be distributed.

#### NUMBC

This is the total number of applied point loads at nodal points. You must later specify the x and y coordinates of these applied loads.

#### NODAL POINT DATA

This input is used to dimension the size of the level 0 triangle. The x and y coordinates of the three nodal points defining the level 0 triangle are input. The input is in the order, nodal point 1, nodal point 2, and nodal point 3.

#### NODAL POINT BOUNDARY CONDITIONS

This line is used to specify the nodal point number and the x and y components of the applied load at that nodal point number.

There is one line for the value input for NUMBC. That is, if NUMBC = 2, then two nodal points have an applied load, thus that nodal point and its corresponding load is input using this card.

#### MATERIAL PROPERTY DATA

For each of the specified number of different materials, NMAT, each of the following must be input: N (material number), EL (elastic modulus), ENU12 (Poisson's ratio), and RO (density).

EXAMPLE INPUT/OUTPUT

Consider a triangular plate with a 1000 pound load in the X-direction applied at nodal point 1 as shown in Figure C1. The boundary conditions are such that the base is clamped, and all other surfaces are free to move in the x and y directions. The plate is made of one materials with the following properties:

$$EL = .2 \times 10^8 \text{ psi}$$

$$ENU12 = .21$$

$$RO = .5$$

Solving this problem with a level 2 fractal finite element mesh would require the input cards shown in Table C1.

TABLE C1. Example computer input.

EXAMPLE

|    |           |       |      |     |    |      |    |  |
|----|-----------|-------|------|-----|----|------|----|--|
| 1  |           |       |      |     |    |      |    |  |
| 2  | 3         | 3     | 0    | 1   |    |      |    |  |
| 11 |           | 0.    |      | 0.  |    |      |    |  |
|    | 50.       | 70.71 |      | 0.  | 0. | 100. | 0. |  |
| 1  | 1000.     |       | 0.   |     |    |      |    |  |
| 1  | 20000000. |       | 0.21 | 0.5 |    |      |    |  |
| 2  | 20000000. |       | 0.21 | 0.5 |    |      |    |  |
| 3  | 20000000. |       | 0.21 | 0.5 |    |      |    |  |

The computer output would be as shown in Tables C2 through C6. The first information output is a reflection of input data as given in Table C2.

TABLE C2. Computer output reflecting input data.

TITLE:EXAMPLE

```

NUMBER OF LEVELS           :LEVEL = 2
PROBLEM                    :PROB = 1
NUMBER OF ELEMENT          :NUMEL = 16
NUMBER OF MATERIALS        :NMAT = 3
NUMBER OF NODAL POINTS    :NUMNP = 15
NUMBER OF PRESSURE CARDS   :NPC = 0
NUMBER OF SPECIFIED LOADS  :NUMBC = 1
BOUNDARY TYPE :LTYPE       :LTYPE = 3

```

The next section of output shows the connectivity of the nodal points with the appropriate elements as shown in Table C3.

TABLE C3. Element connectivity output.

| ELEMENT NUMBER | I  | J  | K  | TYPE |
|----------------|----|----|----|------|
| 1              | 1  | 2  | 3  | 1    |
| 2              | 2  | 4  | 5  | 1    |
| 3              | 4  | 7  | 8  | 1    |
| 4              | 7  | 11 | 12 | 1    |
| 5              | 3  | 5  | 6  | 1    |
| 6              | 5  | 8  | 9  | 3    |
| 7              | 8  | 12 | 13 | 1    |
| 8              | 6  | 9  | 10 | 1    |
| 9              | 9  | 13 | 14 | 1    |
| 10             | 10 | 14 | 15 | 1    |
| 11             | 2  | 5  | 3  | 2    |
| 12             | 4  | 8  | 5  | 3    |
| 13             | 7  | 12 | 8  | 2    |
| 14             | 5  | 9  | 6  | 3    |
| 15             | 8  | 13 | 9  | 3    |
| 16             | 9  | 14 | 10 | 2    |

The nodal point coordinates along with the specified applied loads are printed next as shown in Table C4.

TABLE C4. Nodal point coordinate computer output.

| ...NODAL POINT COORDINATES... |      |           |          |  |
|-------------------------------|------|-----------|----------|--|
| NODAL POINT NUMBER            | TYPE | X-COORD   | Y COORD  |  |
| 1                             | 0    | 50.00000  | 70.71000 |  |
| 2                             | 0    | 37.50000  | 53.03250 |  |
| 3                             | 0    | 62.50000  | 53.03250 |  |
| 4                             | 0    | 25.00000  | 35.35500 |  |
| 5                             | 0    | 50.00000  | 35.35500 |  |
| 6                             | 0    | 75.00000  | 35.35500 |  |
| 7                             | 0    | 12.50000  | 17.67750 |  |
| 8                             | 0    | 37.50000  | 17.67750 |  |
| 9                             | 0    | 62.50000  | 17.67750 |  |
| 10                            | 0    | 87.50000  | 17.67750 |  |
| 11                            | 11   | 0.00000   | 0.00000  |  |
| 12                            | 11   | 25.00000  | 0.00000  |  |
| 13                            | 11   | 50.00000  | 0.00000  |  |
| 14                            | 11   | 75.00000  | 0.00000  |  |
| 15                            | 11   | 100.00000 | 0.00000  |  |

BANDWIDTH = 12

| NODAL POINT NUMBER | X-BOUNDARY VALUE | Y-BOUNDARY VALUE |
|--------------------|------------------|------------------|
| 1                  | 0.100000E+04     | 0.000000E+00     |
| 2                  | 0.000000E+00     | 0.000000E+00     |
| 3                  | 0.000000E+00     | 0.000000E+00     |
| 4                  | 0.000000E+00     | 0.000000E+00     |
| 5                  | 0.000000E+00     | 0.000000E+00     |
| 6                  | 0.000000E+00     | 0.000000E+00     |
| 7                  | 0.000000E+00     | 0.000000E+00     |
| 8                  | 0.000000E+00     | 0.000000E+00     |
| 9                  | 0.000000E+00     | 0.000000E+00     |
| 10                 | 0.000000E+00     | 0.000000E+00     |
| 11                 | 0.000000E+00     | 0.000000E+00     |
| 12                 | 0.000000E+00     | 0.000000E+00     |
| 13                 | 0.000000E+00     | 0.000000E+00     |
| 14                 | 0.000000E+00     | 0.000000E+00     |
| 15                 | 0.000000E+00     | 0.000000E+00     |

Note that nodal points 11, 12, 13, 14, and 15 all have constraint code 11; i.e., a clamped boundary condition. Also note that nodal point a has 1 1000 pound load in the x direction. All other nodes are load free.

Next, the material properties are printed as shown in Table C5.

TABLE C5. Computer output of input material properties.

...MATERIAL PROPERTIES AS INPUT...

|                     |               |
|---------------------|---------------|
| MATERIAL SET NUMBER | = 1           |
| YOUNG'S MODULUS     | = 0.20000E+08 |
| POISSON'S RATIO     | = .21000E+00  |
| RO                  | = 0.50000E+00 |
| MATERIAL SET NUMBER | = 2           |
| YOUNG'S MODULUS     | = 0.20000E+08 |
| POISSON'S RATIO     | = .21000E+00  |
| RO                  | = 0.50000E+00 |
| MATERIAL SET NUMBER | = 3           |
| YOUNG'S MODULUS     | = 0.20000E+08 |
| POISSON'S RATIO     | = .21000E+00  |
| RO                  | = 0.50000E+00 |
| MEQ                 | = 30          |

Finally, the displacements of the nodes are printed out as shown in Table C6.

TABLE C6. Computer output of displacement fields.

\*\*\*\*\*DISPLACEMENT FIELDS\*\*\*\*\*

| NODE NUMBER | U-DISPLACEMENT | V-DISPLACEMENT  |
|-------------|----------------|-----------------|
| 1           | 0.51199842E-03 | 0.70529661E-36  |
| 2           | 0.22070234E-03 | 0.84979411E-04  |
| 3           | 0.22070234E-03 | -0.84979411E-04 |
| 4           | 0.93007222E-04 | 0.68186471E-04  |
| 5           | 0.90687200E-04 | 0.27330244E-36  |
| 6           | 0.93007222E-04 | -0.68186471E-04 |
| 7           | 0.32604130E-04 | 0.30737738E-04  |
| 8           | 0.29193780E-04 | 0.17358664E-04  |
| 9           | 0.29193780E-04 | -0.17358664E-04 |
| 10          | 0.32604130E-04 | -0.30737738E-04 |
| 11          | 0.00000000E+00 | 0.00000000E+00  |
| 12          | 0.00000000E+00 | 0.00000000E+00  |
| 13          | 0.00000000E+00 | 0.00000000E+00  |
| 14          | 0.00000000E+00 | 0.00000000E+00  |
| 15          | 0.00000000E+00 | 0.00000000E+00  |

Notice that the clamped edge (nodal points 11 through 15) have zero displacements.

## TYPICAL APPLICATIONS

Six examples given below demonstrate that the responses of the fractal mesh are different for nonhomogeneous and weighted average homogeneous material properties. The materials properties are given in Tables D1 and D2.

The numerical results are for vertical displacements under a vertical concentrated load of 1000 pounds. The results for fractal mesh generation levels 3, 4 and 5 are compared with a weighted homogeneous average approach in Table D3. Case I is for an analysis considering the nonhomogeneous fractal mesh; whereas, Case II uses weighted average homogeneous moduli. In addition, the results for both cases are verified using a conventional finite element program [Sandhu, 1983].

TABLE D1. Nonhomogeneous material properties.

| MATERIAL NO. | MATERIAL PROPERTIES |                 |
|--------------|---------------------|-----------------|
|              | Young's Modulus     | Poisson's Ratio |
| 1            | 0.20000000E+08      | 0.21            |
| 2            | 0.22000000E+08      | 0.21            |
| 3            | 0.24000000E+08      | 0.21            |
| 4            | 0.26000000E+08      | 0.21            |
| 5            | 0.28000000E+08      | 0.21            |
| 6            | 0.30000000E+08      | 0.21            |

TABLE D2. Weighted average moduli.

| LEVEL | MATERIAL PROPERTIES |                 |
|-------|---------------------|-----------------|
|       | Young's Modulus     | Poisson's Ratio |
| 3     | 0.22531250E+08      | 0.21            |
| 4     | 0.23898437E+08      | 0.21            |
| 5     | 0.2542328E+08       | 0.21            |

TABLE D3. Vertical displacements at top of gasket.

| METHOD | Fractal Mesh  |               | PLSTR [Sandhu, 1983]] |               |
|--------|---------------|---------------|-----------------------|---------------|
|        | Case I        | Case II       | Case I                | CaseII        |
| 3      | 0.7087927E-03 | 0.6503804E-03 | 0.7087926E-03         | 0.6503800E-03 |
| 4      | 0.9111827E-03 | 0.8100653E-03 | 0.9111825E-03         | 0.8100651E-03 |
| 5      | 0.1104476E-03 | 0.9496508E-03 | 0.1104477E-03         | .9496507E-03  |

## DISTRIBUTION LIST

**AUL/LSE**

**Bldg 1405 - 600 Chennault Circle  
Maxwell AFB, AL 36112-6424 1 cy**

**DTIC/OCP**

**8725 John J. Kingman Rd, Suite 0944  
Ft Belvoir, VA 22060-6218 2 cys**

**AFSAA/SAI**

**1580 Air Force Pentagon  
Washington, DC 20330-1580 1 cy**

**PL/SUL**

**Kirtland AFB, NM 87117-5776 2 cys**

**PL/HO**

**Kirtland AFB, NM 87117-5776 1 cy**

**Official Record Copy**

**PL/WST/David Crook 1 cy**